Emission measurements and in-situ observation of ionic liquid electrospray thrusters with longitudinally grooved emitters

Koki Matsukawa[1], Yuiko Nakashima[1], Momoko Naemura[1] and Yoshinori Takao[2*]

*Correspondence:
takao@ynu.ac.jp

[1] Department of Mechanical Engineering, Materials Science, and Ocean Engineering, Yokohama National University, Yokohama, Kanagawa 240–8501, Japan
[2] Division of Systems Research, Yokohama National University, Yokohama, Kanagawa 240–8501, Japan

Abstract

An externally wetted emitter array with longitudinally grooved structures for ionic liquid electrospray thrusters was fabricated to improve ionic liquid transport to the emitter tips. Two grooved emitter shapes with different groove depths were successfully fabricated using microelectromechanical system processing techniques. We evaluated the current–voltage characteristics, measured the mass spectra using time-of-flight (ToF) spectrometry, and conducted in-situ observations using a high-speed microscope. The experimental results of ion emission show that the absolute emission current increases compared with that of our previous emitter without grooves. This tendency is strengthened with deeper grooves. Moreover, the slope of the current–voltage curve for the grooved emitters does not decrease even when high voltages are applied, indicating that the grooved structure improves the ionic liquid transport to the emitter tips. This improvement is attributed to the low hydraulic impedance of the emitter structure. However, deeper grooving also increases the percentage of current intercepted by the extractor electrode, and electrochemical reactions are not avoided at an alternation frequency of 1 Hz. Although the first current–voltage measurement tended to have unstable characteristics, the ToF results indicated that the emission in the center line was in the pure-ion regime, composed mostly of monomer and dimer ions, under all the measured conditions. High-speed microscope observations showed that too much ionic liquid deposited on the extractor causes ion emission from the extractor to the emitter, known as backspray, and implies that no large droplets are emitted for either grooved emitter structure, which is consistent with the ToF results.

Keywords: Electrospray, Externally wetted, Microfabrication, Ionic liquid, Time-of-flight, High-speed imaging

Matsukawa *et al. Journal of Electric Propulsion*   (2023) 2:23

Page 2 of 28

Introduction

In recent years, various advanced space missions that require precise control of the spacecraft attitude and position have been proposed [1–4]. For example, space gravitational wave observatories are currently under development to detect low-frequency gravitational waves that are difficult to observe on Earth because of noise and size limitations. In the mission, three spacecraft will perform formation flights and detect picometer-level changes in the arm lengths between them, where each spacecraft must operate "drag-free" against any disturbances. Thrusters with precise thrust control to maintain the relative positions of the satellite formation are required for such missions [5, 6]. Additionally, the number of launched microspacecraft has greatly increased, and the need for a propulsion system that can be mounted on such micro/nanosatellites is growing. Missions for formation flights, constellations, and deep space exploration have been proposed and conducted using microspacecraft or CubeSats [7–9].

For such advanced missions and microspacecraft, ionic liquid electrospray thrusters (ILESTs) have attracted attention as miniature electric propulsion systems that can precisely control thrust because they require neither gas propellants nor neutralizers (electron sources) [10–17]. Figure 1 illustrates a schematic of the electrospray thruster. Electrospray thrusters are composed of an emitter chip with many emitters on its surface and an opposing extractor electrode. The ionic liquid, which is the propellant of the thruster, is transported to the emitter tips by applying high voltages of several kilovolts between the emitters and extractor electrodes. A strong electric field is generated at the emitter tips because the radius of curvature of the emitter tips is only a few micrometers. This strong electric field transforms the ionic liquid into a conical structure called a Taylor cone [18, 19], and ions are extracted from the ionic liquid when the liquid interface achieves a mechanical balance between the forces of electrical traction and surface tension [20–22]. The extracted ions are then accelerated by the electric potential difference between the emitters and extractor electrode to generate a small amount of thrust per emitter.

Ionic liquids are molten salts consisting only of cations and anions and have almost zero vapor pressure due to the Coulomb force between cations and anions [23]. Thus, ionic liquids can exist as a liquid phase even in vacuum and eliminate the need
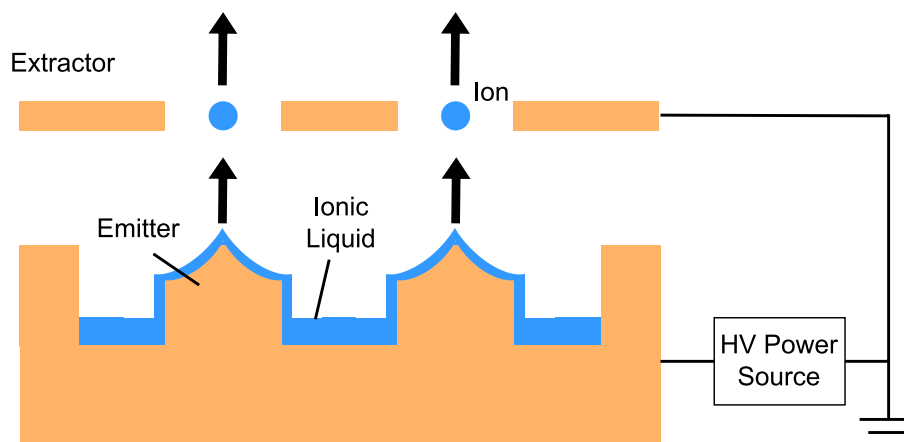

Fig. 1 Schematic of the externally wetted electrospray thruster

for high-pressure gas feed systems, including gas valves with the mechanical vibration required for conventional electric propulsion systems. Because ILESTs can emit cations and anions by applying positive and negative voltages, neutralizers can also be eliminated from the propulsion system, where electrons do not produce thrust while anions do. Moreover, the thrust can be precisely controlled by adjusting the number of emitters and applied voltage because only a small amount of thrust (on the order of 10 nN in the pure-ion mode) per emitter is provided [24, 25]. These features further contribute to miniaturizing propulsion systems and enabling the precise control of satellites.

Electrospray thrusters typically have three types of emitter structure: internally fed capillary, porous, and externally wetted. The Laser Interferometer Space Antenna (LISA) Pathfinder mission employed internally fed capillary emitters, where the flow rate of the ionic liquid was actively controlled and charged droplets were emitted [26]. It is difficult for capillary emitters to emit ions in a purely ionic regime without charged droplets because of the low fluidic impedance of the capillary [15, 27]. Porous emitters are currently the most popular structures, and many studies have been conducted [13, 16, 17, 24, 28–31]. The ionic liquid is passively supplied by the capillary force of the tiny pores. Ion emission can be operated in the purely ionic regime, where the emission occurs without any large cluster ions or charged droplets, but porous emitters inherently have non-uniformities on the emitter surface because of the random pore sizes. Externally wetted emitters can be fabricated using a technique to fabricate silicon-based microelectromechanical system (MEMS) devices, and this fabrication process can uniformly control the emitter structures. This emitter type can also produce ion emissions in the purely ionic regime [11, 32]; thus, the thrust can be controlled more precisely because of the significantly low mass of ions compared with that of droplets.

In our previous studies, we fabricated two types of silicon-based emitter arrays using microfabrication techniques: one to improve the thrust density with a massive capillary emitter array [33–35], and the other to realize precise thrust control with an externally wetted emitter array [36]. In this study, we focused on the latter case. In our previous study, we successfully fabricated uniform needle emitter arrays and conducted ion emission experiments [36]. Ion-emission experiments showed that the ion currents per emitter were almost identical at the same applied voltage, even for emitter chips with different numbers of emitters, indicating that the number of emitters can be used to control the ion current. However, insufficient ionic liquid transport to the emitter tips was implied, because the slopes of the current–voltage curves decreased at high voltages on both the positive and negative sides. For precise thrust control, it is necessary to extract a stable ion current from the emitter array.

We fabricated externally wetted emitters with a longitudinally grooved structures to improve the transport of the ionic liquids to the emitter tips. Moreover, we evaluated the current–voltage characteristics and measured the mass spectra using ToF spectrometry. To investigate the effects of grooving, we prepared two types of emitter structures: shallow and deep grooves. Longitudinally grooving the emitter significantly improves the emission current for both emitter types, where the emission in the center line was indicated to be in the pure-ion regime with the ToF measurements. However, the current–voltage characteristics tended to be unstable during the first measurement, where

abrupt current increases sometimes occurred at the emitter and extractor electrodes. We also observed the electrospray emissions using a high-speed microscope to investigate this phenomenon. Although less than a few micrometers cannot be observed due to the resolution limitation of the present optical microscope, unstable emission involves large droplets and off-axis or intermittent cone-jet pulsation, which were observed with a microscope for capillary emitters [37–39]. Microscopic imaging was also employed to observe emission sites in a porous emitter [40] and to estimate the mass flow rate in an externally wetted emitter [41].

The remainder of this paper is organized as follows. Section "Fabrication of the emitter chip" describes the fabrication process and presents the fabricated emitter arrays with and without an ionic liquid supply system. Section "Experimental setups" introduces the experimental setup for the current–voltage characteristics, ToF measurement system, and high-speed microscopic observations. Section "Results and discussion" presents the experimental results and discussions, including the dependence of each emitter on the hydraulic impedance, explaining the emission current improvement, and the effect of the electrochemical reaction. Finally, Section "Conclusions" presents the conclusion in the study.

Fabrication of the emitter chip

Fabrication process of the emitters

We fabricated an emitter chip with an array of grooved needle emitters using a technique used to fabricate MEMS devices. Figure 2 shows the emitter fabrication process; the process flow is identical to that described in our previous study [36]. First, the silicon wafer was coated with a positive-type photoresist (AZ P4620). This photoresist was exposed via laser direct writing (Fig. 2a) and developed to produce a photoresist pattern that became an etching mask (Fig. 2b). Figure 3 shows a schematic diagram of the etching mask. A star-shaped etching mask was used to fabricate grooves on the emitter side surface. These dimensions will be described later. Second, the cone-shaped emitter tips were fabricated by isotropic etching using SF_6, based on a patterned star-shaped
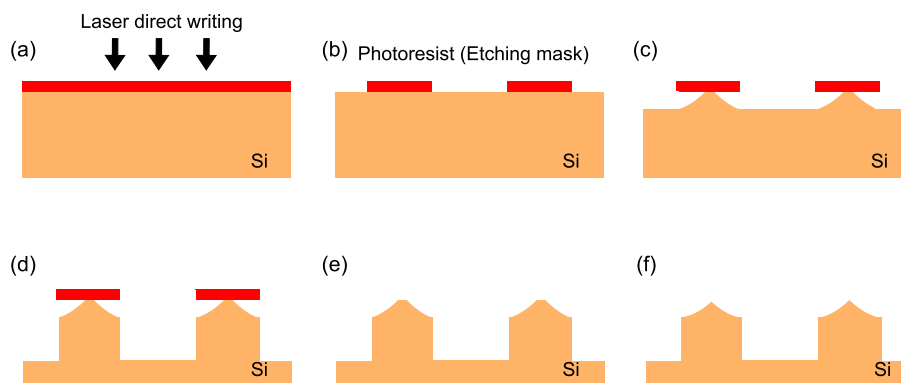

Fig. 2 Fabrication process for emitter arrays. **a** Silicon wafer coated with a positive-type photoresist (AZ P4620) is exposed by a laser direct writing, and **b** the photoresist was developed, where the patterned photoresist became an etching mask. **c** Isotropic etching using SF_6 and **d** anisotropic etching using the Bosch process were conducted. **e** The photoresist was removed from the emitter tips. **f** The emitter tips were sharpened by isotropic etching again
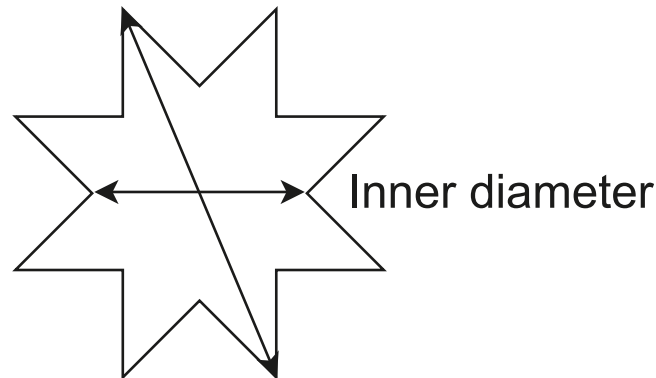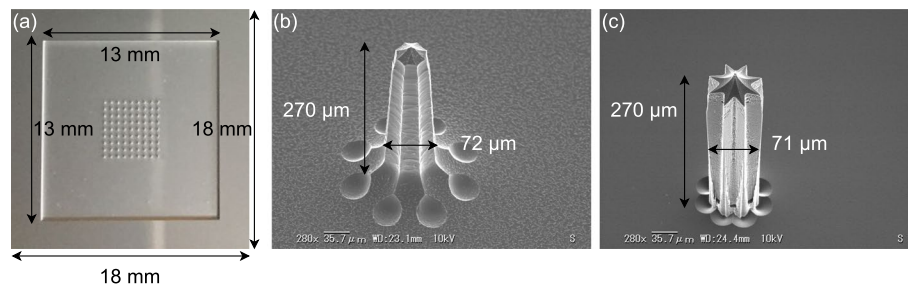
Fig. 3 Schematic of the etching mask

Fig. 4 **a** Photograph image of a fabricated emitter chip with 81 emitters. SEM images of **b** the shallow-grooved emitter and **c** the deep-grooved emitter

photoresist (Fig. 2c). Then, ionic liquid reservoir was formed via anisotropic etching using the Bosch process [42, 43], as shown in Fig. 2d. After removing the photoresist (Fig. 2e), the emitter tips were sharpened via isotropic etching again (Fig. 2f).

Figure 4a shows the emitter chip fabricated using the aforementioned fabrication process. The emitter chip is 18 mm square and encompasses an array of 81 (9 × 9) emitters with a pitch of 500 μm, fabricated within a 13×13 mm^2 ionic liquid reservoir area in the center of the chip. We fabricated two types of emitters with different groove depths by varying the mask size and isotropic etching time. Figure 4b shows the emitter with shallow grooves using the etching mask with an outer diameter of 200 μm and an inner diameter of 100 μm. The first isotropic etching (Fig. 2c) was performed for 500 s, and the second isotropic etching (Fig. 2f) was performed for 440 s. Figure 4c shows the emitter with deep grooves using the etching mask with an outer diameter of 100 μm and an inner diameter of 50 μm. The first isotropic etching (Fig. 2c) was conducted for 275 s, and the second isotropic etching time (Fig. 2f) was 50 s. We successfully fabricated two types of emitters with almost the same diameters but different groove depths by adjusting them. Notably, the second isotropic etching was intended to sharpen the emitter tips. Consequently, the emitter height slightly decreased from the top surface of the silicon wafer (up to approximately 40 μm from the time and rate of the isotropic etching). In our previous study, the second isotropic etching time was 662 s; thus, the gap between the
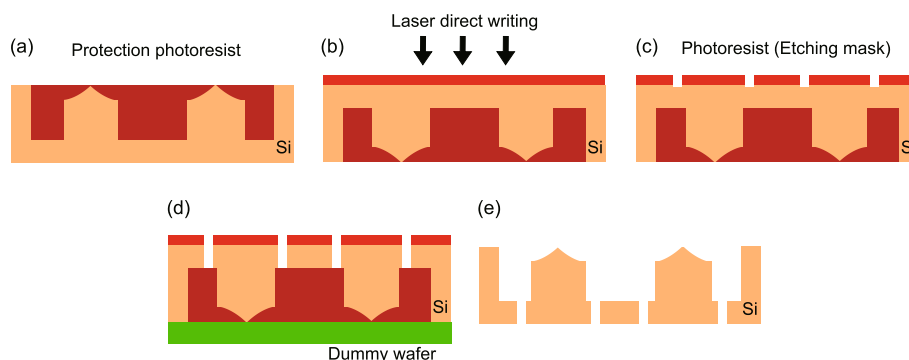
Fig. 5 Fabrication process of the ionic liquid supply holes from the back side. **a** Photoresist (7790G-27CP) was coated to protect front-side emitters. **b** A coated photoresist (AZ P4620) on the back side was exposed by a laser direct writing and **c** developed. **d** Anisotropic etching using the Bosch process was conducted to fabricate through holes. **e** The dummy wafer and resists were removed from the silicon wafer
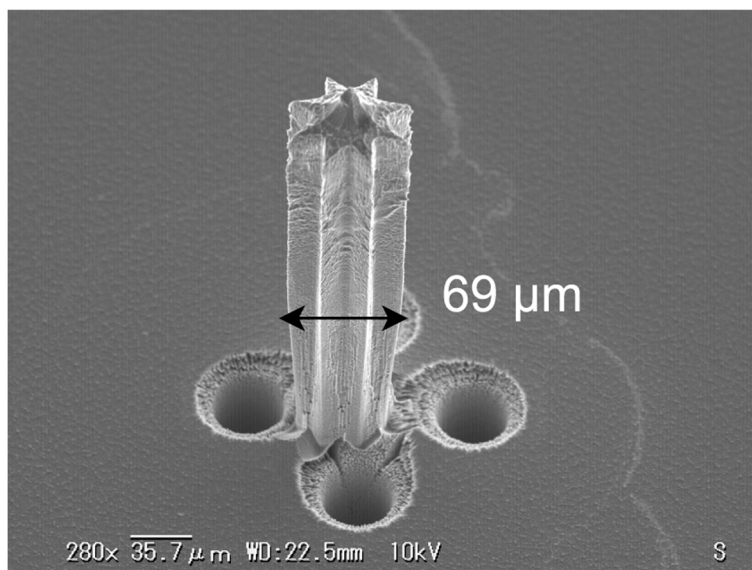

Fig. 6 SEM image of the deep-grooved emitter with four through holes at the emitter base

emitter tip and the extractor decreased in the order of non-grooved, shallow-grooved, and deep-grooved emitters, even though the gap between the top surface of the emitter chip and the bottom surface of the extractor was fixed.

Fabrication process of ionic liquid supply holes

Figure 5 shows the fabrication process of the ionic liquid supply system, which is necessary for continuous ionic liquid replenishment. After the emitter fabrication on the front side, the wafer was coated with a photoresist (7790G-27CP) to protect the emitters, as shown in Fig. 5a. The back side of the wafer was coated with a positive-type photoresist (AZ P4620). After patterning the back-side photoresist layer similarly to the front side, we fabricated through-holes at the emitter base using the Bosch process, as shown

in Fig. 5b-d. An aluminum-deposited dummy wafer protects the surface emitters from etching. After removing the dummy wafer, the photoresist on both the front and back sides was eliminated, as shown in Fig. 5e. Figure 6 shows an SEM image of the fabricated deep-grooved emitter with four through-holes at the emitter base to supply ionic liquid from the back side of the emitter chip. The diameter of through-holes at the base of the emitter was 30 μm. The fabrication process of the front-side emitters was the same as that of the emitter, as shown in Fig. 4c.

Experimental setups

Current measurements without an ionic liquid supply system

Figure 7 shows the experimental setup used to measure the ion emission current. In this setup, we tested emitter chips without an ionic liquid supply system fabricated using only the front-side process described in Section "Fabrication process of the emitters". We prepared the emitter chips with an array of 81 emitters and dropped 0.01 μl 1-ethyl-3-methylimidazolium dicyanamide (EMI-DCA) as the propellant onto the emitter chips. Notably, 0.01 μl is the minimum amount measured with a micropipette employed. Before supplying with ionic liquid, the fabricated chip was exposed to atmospheric pressure helium plasma discharge, improving the wettability of the ionic liquid on the Si surface [44]. Here, EMI-DCA tends to emit ions in the purely ionic regime and is a propellant candidate for electrospray thrusters [45, 46].

The distance between the top surface of the emitter chip and the bottom surface of the extractor electrode, or the gap distance, was set at $d = 0.4$ mm, and the extractor electrode had an aperture of $\varphi = 0.4$ mm in diameter. Similar to our previous study, an extractor electrode was fabricated by etching a silicon wafer, and the emitter chip and extractor electrode were aligned using an assembled device [36]. A stainless-steel plate was used as the collector electrode and was placed downstream of the emitter array to measure the ion current. These electrodes were set in a vacuum chamber exhausted by a dry pump and a turbomolecular pump at a pressure of less than 2.0×10^{-3} Pa.
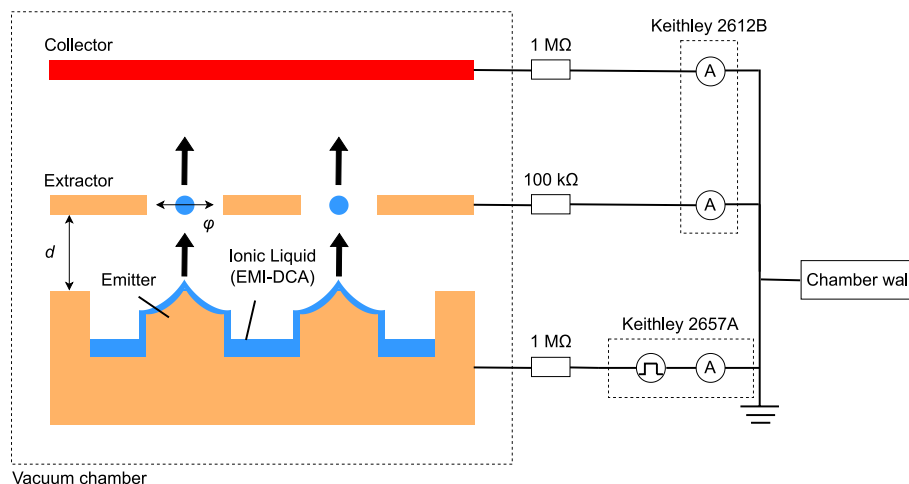

Fig. 7 Schematic of the experimental setup for ion current measurements without an ionic liquid supply system, where *d* and *φ* are the distance between the emitter and extractor electrode and the hole diameter of the extractor, respectively

The emitter chip could be biased from 0 to ± 3000 V using a source meter (Keithley, 2657A) through a 1 MΩ resistor. The extractor and collector electrodes were connected to another source meter (Keithley, 2612B) through 100 kΩ and 1 MΩ resistors, respectively. These resistors are used for source meter protection. A bipolar pulse voltage of 1 Hz was applied to the emitter, and the output voltages to the extractor and collector electrodes were set to 0 V (equivalent to the ground and chamber potentials). The voltage step was set to be ± 100 V in the range between 0 and ± 1500 V and ± 10 V in the range between ± 1500 and ± 3000 V. The current value was obtained by averaging 30 measurement points per voltage value, and the measurement interval was set to 10 ms.

In this system, the ionic liquid occasionally exhibited an overabundance; thus, the first current–voltage measurement tended to show unstable characteristics (e.g., a large extractor current was observed). Secondary species emissions (SSEs) produced by the impact of high-energy ions on the chamber walls and collector surfaces can lead to unreliable measurements during ground testing [47]. However, we employed a source meter that can precisely measure the tiny DC currents of emitters at high voltages, and focused on the emitter and extractor currents in this study. Although the collector currents were treated as references, we confirmed that the sum of the emitter and extractor currents was approximately equal to the collector currents.

Current measurements with an ionic liquid supply system

Figure 8 shows the experimental setup for the emitter chips with an ionic liquid supply system fabricated using the process described in Sections "Fabrication process of the emitters" and "Fabrication process of ionic liquid supply holes". This experimental setup was almost the same as that described in Section "Current measurements without an ionic liquid supply system"; however, the ionic liquid was supplied from the back side of the emitter chip by installing a tank with a sponge absorbing sufficient ionic liquid
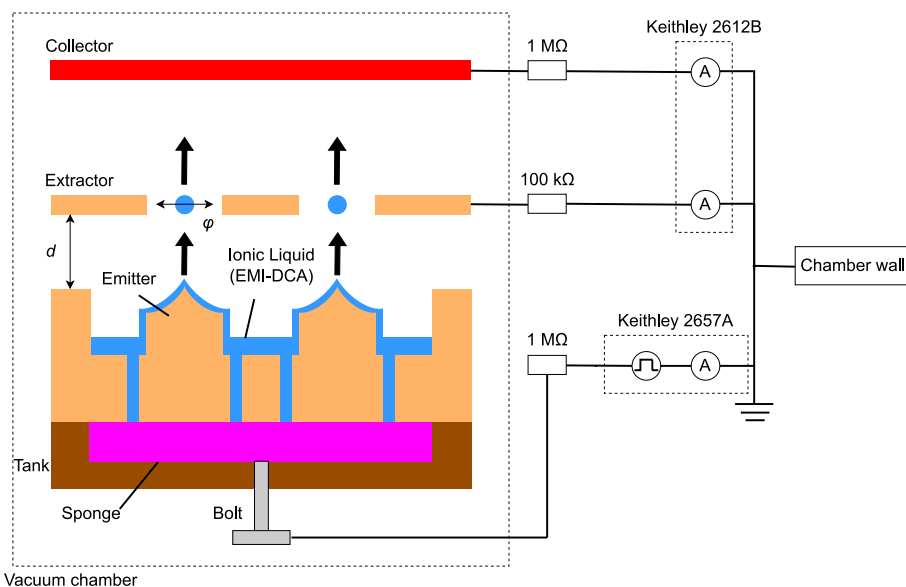

Fig. 8 Schematic of the experimental setup for ion current measurements supplying ionic liquid from the back side of the emitter chip, where d and φ are the distance between the emitter and extractor electrode and the hole diameter of the extractor, respectively

(EMI-DCA) on the back side of the emitter chip and fixing it with a bolt. The sponge used in this experiment was a commercially available dishwashing sponge made of polyurethane foam that was cut to fit the tank size. A voltage was applied to the ionic liquid through this bolt. The diameter of through-holes (30 µm) was much smaller than the pore diameter of the sponge, allowing ionic liquid to be supplied to the emitter by capillary force. However, the flow rate of the ionic liquid was not actively controlled.

Time-of-flight mass spectrometer

Figure 9 shows the setup for ToF mass spectrometry using a high-speed current amplifier, similar to the setup employed previously in electrospray experiments [16, 30, 48, 49]. The system was placed downstream of the thruster and consisted primarily of a gate electrode to deflect the ion beams and a downstream collector. A cylindrical grounded shield made of stainless steel with a diameter of 10 mm and length of 441 mm was installed upstream of the collector. The ToF gate consisted of an upstream aluminum plate with an aperture of 5 mm in diameter, two copper electrodes as a deflector, and a downstream aluminum plate with an aperture of 1 mm in diameter. The distance between the two aluminum plates was 28 mm. Only one copper electrode was biased to a high voltage, whereas the others were grounded (equivalent to the chamber potential). The high-voltage pulse was supplied using a custom-made pulse generator (ART, MPG-1502) connected to a DC high-voltage source (Matsusada Precision, HJPM-3R5) and a function generator (GW Instek, AFG-3032). A square wave consisting of 0 and 1000 V for a duration of 500 µs was applied to the copper gate electrode at 100 Hz with both rise and fall times less than 80 ns.

ToF experiments were conducted at a distance $L = 527$ mm between the gate electrode and the collector. The thruster was located 35 mm upstream from the ToF gate. The ToF collector current was converted to voltage using a high-speed current amplifier (FEMTO, DHPCA-100) with a gain of 10^6 V/A and a bandwidth of 1 MHz. The amplified voltage was recorded and averaged over 300 cycles by using an oscilloscope (Tektronix,
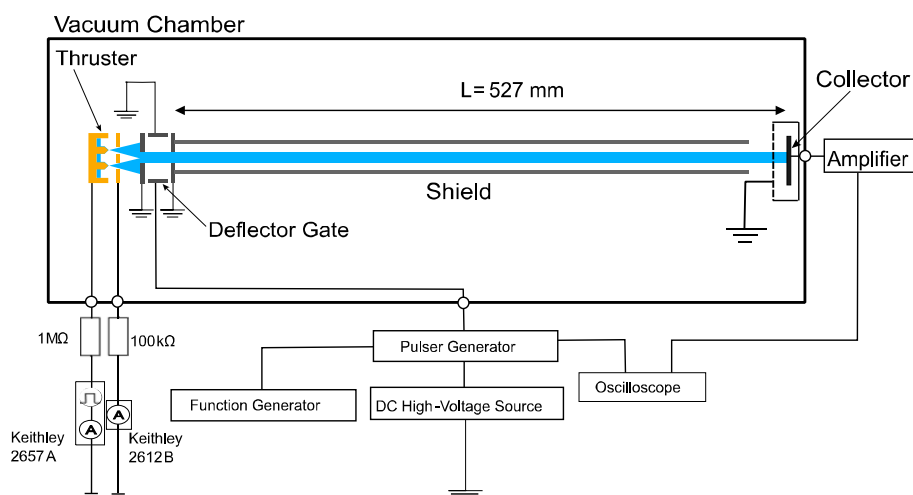

Fig. 9 Schematic of the experimental setup for the ToF mass spectrometry using a high-speed current amplifier, where $L = 527$ mm is the distance between the deflector gate and the collector

MSO46 4-BW-200) to improve the signal-to-noise ratio. The mass of the ions was calculated by measuring the time traveled from the gate electrode to the collector, where singly charged ions were assumed.

To investigate the difference in beam compositions between the shallow- and deep-grooved emitters, we used the same emitter chips without the ionic liquid supply system as in Section "Current measurements without an ionic liquid supply system" and dropped 0.01µl EMI-DCA as the propellant onto the 81-emitter chip. We also employed the same extractor electrode as in Section "Current measurements without an ionic liquid supply system", where the aperture was $\varphi = 0.4$ mm in diameter, and the gap distance was set at $d = 0.4$ mm. The ToF measurements were conducted at pressures below 4×10^{-4} Pa in a smaller chamber than that was used for the current–voltage measurements. The emitter chip was biased using a source meter (Keithley, 2657A) through a 1 MΩ resistor, and the extractor electrode was connected to another source meter (Keithley, 2612B) through 100 kΩ. Notably, the present ToF system can measure the signal only at the center line of the beams.

Emission observation with a high-speed microscope

To investigate the characteristics of the ion emissions, we conducted in-situ observations of the electrospray thruster using a high-speed microscope (Keyence, VW-9000) with a long-distance and 500-power magnifying lens (Keyence, VH-Z50). Figure 10a shows the experimental setup for the observation, where the emitter and extractor electrodes were placed in a small vacuum chamber with a diameter of 40 mm and length of 50 mm. The high-speed microscope was placed outside the vacuum chamber, 85 mm from the emitter tip. A continuous light source was placed outside the chamber on the opposite side of the microscope. Shadow images of the emitter tip were recorded at a frame rate of 1000 fps and a shutter speed of 1/4000–1/3000 s. If the thruster is operated in the purely ionic regime, ion emission cannot be observed using a high-speed microscope, which is far below the diffraction limit for optical microscopy. Nonetheless, the microscope can observe such phenomena if charged particles are emitted as large droplets (> a few
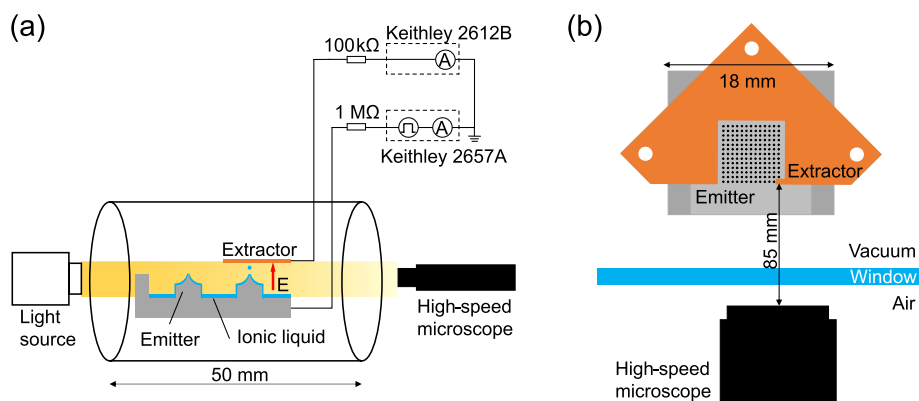

Fig. 10 **a** Experimental setup for high-speed microscope observation of ion emission, and **b** the top view of the 169-emitter array and extractor electrode. Only a single emitter is faced with the extractor, where the ion emission occurs

micrometers in diameter) or if a relatively large volume of ionic liquid is deformed into a Taylor-cone shape.

We cleaved one side of the emitter chip without through-holes to observe the charged particle emission and replaced the extractor electrode with a metal plate without holes. We placed the metal plate such that only the observed emitter faced the extractor electrode, where the ion beam extraction occurred only at the targeted emitter, as shown in Fig. 10b, because the ion emission could be seen only from the emitters in the front row with a high-speed microscope. The easiest way to observe ion emissions is to place the extractor on top of the far-left or far-right emitter in the front row.

In this study, we also used a non-grooved single emitter employed in a previous study as a reference, in addition to 169 shallow-grooved and 169 deep-grooved emitters, to investigate the ion emission phenomena for different emitter structures. We dropped 0.01 and 0.02 μl EMI-DCA as the propellant onto the single and 169-emitter chips, respectively. Some ionic liquid dropped on the single emitter chip was wiped out because the amount of 0.01 μl ionic liquid was considerably large. For the 169-emitter chips, the amount of ionic liquid doubled because of the increase in the number of emitters from 81. Thus, the amount of ionic liquid for each emitter was approximately equal between the 81- and 169-emitter chips, and almost identical ion emissions were expected in the high-speed microscope observations. The distance between the emitter chip and the extractor electrode was set to $d = 0.4$ mm. These electrodes were set in a vacuum chamber exhausted by a rotary pump and a turbomolecular pump at a pressure of less than 1.0×10^{-3} Pa. The emitter chip was biased from 0 to ± 2700 V with a ± 50-V step at a 1-Hz alternation frequency using a source meter (Keithley, 2657 A) through a 1 MΩ resistor, and the extractor plate was connected to another source meter (Keithley, 2612B) through a 100 kΩ resistor. The collector electrode was not used because the extractor had no holes; thus, all the extracted currents were collected through the extractor electrode. The output voltage to the extractor electrode was set as the ground potential, which was equivalent to the chamber potential. The high-speed microscope images were recorded for the voltage range between ± 1700 and ± 2700 V due to the storage limitation at a frame rate of 1000 fps.

Results and discussion

Current–voltage characteristics without an ionic liquid supply system

Figure 11 shows the results of the ion emission experiment of the emitter chip with an array of 81 shallow-grooved emitters (Fig. 4b) and 81 deep-grooved emitters (Fig. 4c) for the first and second voltage applications. The horizontal axis is the voltage applied to the emitter chip, considering the voltage drop across the protective resistor (1 MΩ). Figure 12 presents a typical example of the raw data for Fig. 11b, indicating the data acquisition in the steady-state behavior of ion emission. The transient phenomena due to polarity alternation, observed with an oscilloscope at a high sampling rate [50], were not clearly measured by the source meter because of the low sampling rate.

Figure 11a shows slightly unstable current–voltage characteristics in the first measurement, including a large extractor current on the positive side, compared with the second measurement (Fig. 11b). As shown in Fig. 11b, on the positive side, the onset voltages of ion emission were 1860 V, and the maximum emitter currents reached 219
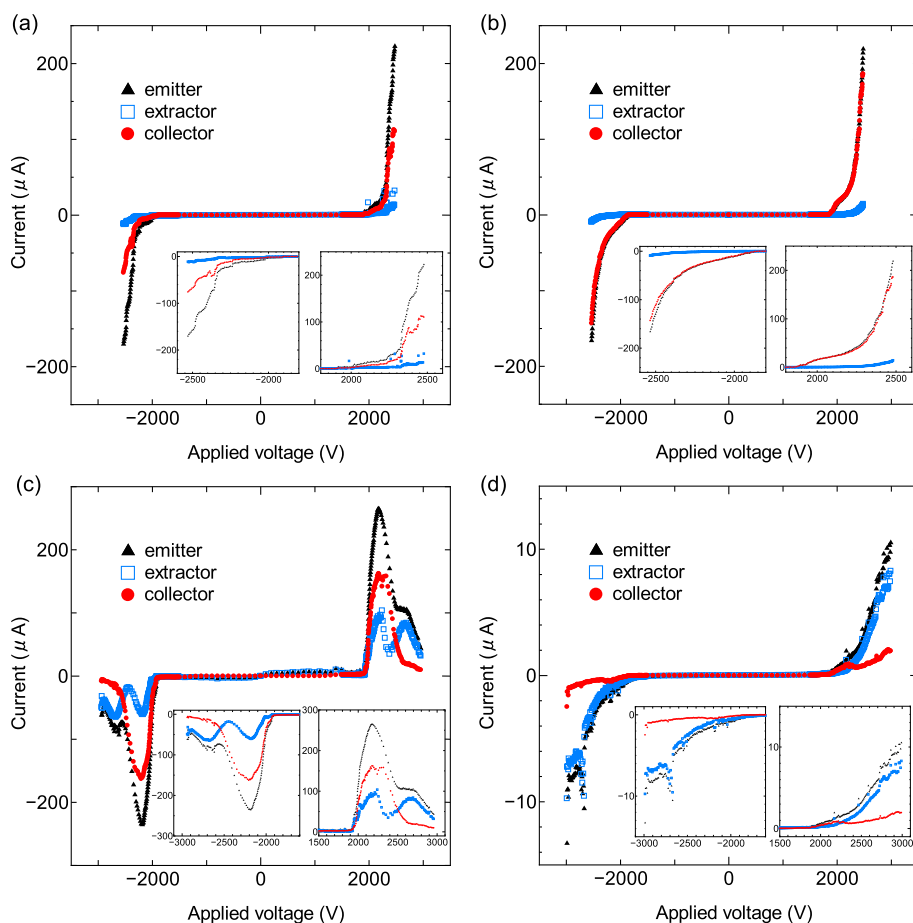
Fig. 11 Emitter, extractor, and collector currents as functions of the applied voltage, where the voltage was determined considering the potential drop through the 1 MΩ resistor. The bottom right insets of each figure represent zoomed views of the non-zero current section parts. **a** The first and **b** second measurements for the shallow-grooved emitter array, and **c** the first and **d** second measurements for the deep-grooved emitter array without the ionic liquid supply system

μA at 2481 V. On the negative side, the onset voltages of ion emission were − 1860 V and the minimum emitter currents reached − 165 μA at − 2534 V. Compared with the previous experimental result with an emitter chip without grooves, where the onset voltages were ± 2040 V and the maximum and minimum emitter currents reached 23 and − 20 μA [36], the absolute extraction onset voltage decreased by approximately 200 V, and the absolute maximum emitter current increased by approximately ten times. The decrease in the onset voltage was partly attributed to the decrease in the distance between the extractor and emitter tip, as described in Section "Fabrication process of the emitters". Additionally, whereas the slopes of the current–voltage curves for non-grooved emitters decreased at approximately ± 2400 V [36], the slope of the current–voltage curve for shallow-grooved emitters did not decrease even when high voltages were applied, as shown in Fig. 11a and b. These results indicate that the grooved structure improved ionic liquid transport to the emitter tips.
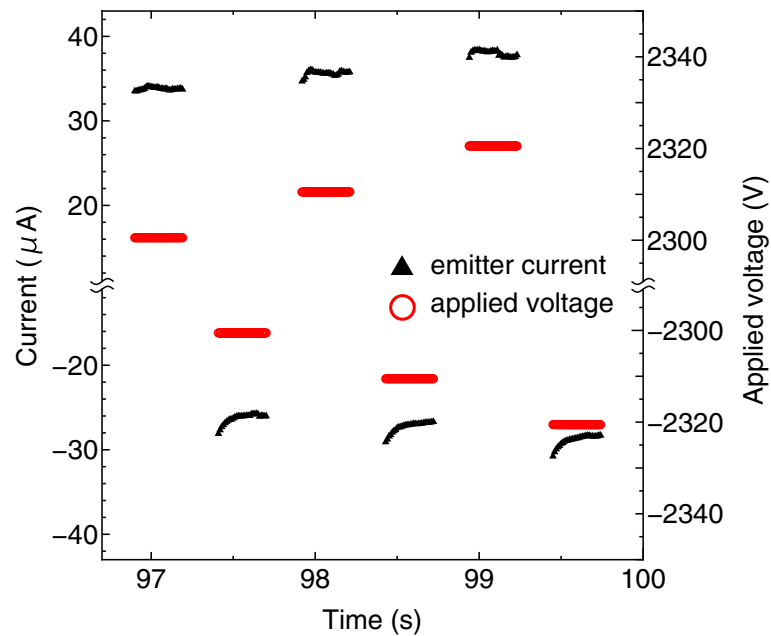
Fig. 12 A typical example of the raw data for Fig. 11b: time variation of emitter current and applied voltage
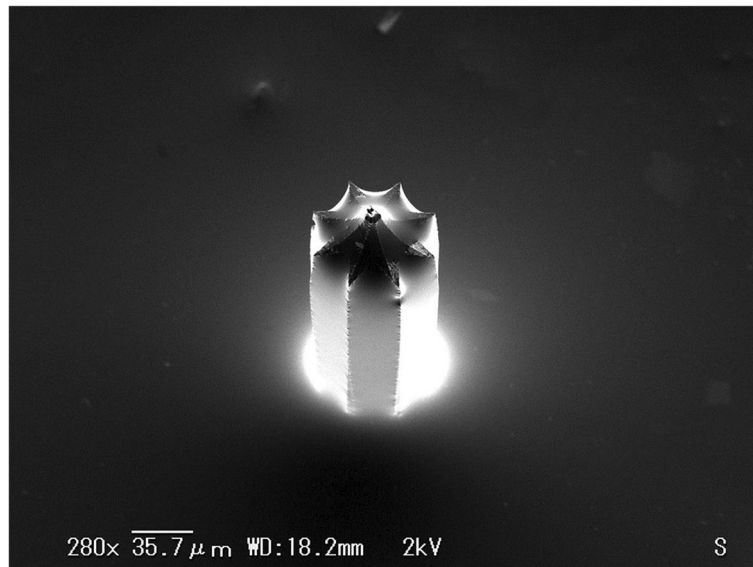

Fig. 13 SEM image of the deep-grooved emitter with a drop of an ionic liquid

Figure 11c shows that the positive emitter current increased to 265 μA at 2175 V and then began to decrease, and the negative emitter current reached −235 μA at −2184 V and then began to fall. Note that Fig. 11c shows the results of the first voltage application. The absolute maximum emitter current of the deep-grooved emitters was more than 12 times larger than that of the shallow-grooved emitters at almost the same voltages (2175 V on the positive side and −2184 V on the negative side). These results indicate that

deepening the grooves further improves the transport capability of the ionic liquid to the emitter tips. Figure 13 shows an SEM image of the fabricated deep-grooved emitter with a drop of an ionic liquid, where the bright part of the SEM image is an ionic liquid. The SEM image also indicates that the deep grooves smoothly transported an ionic liquid to the emitter tips. However, we found that deepening the grooves accelerated ionic liquid consumption and caused depletion of the dropped ionic liquid on the emitter chip. Figure 11d shows the results of the second voltage application. Compared with the first application (Fig. 11c), the current values were significantly reduced, implying depletion of the ionic liquid. An ionic liquid supply system is necessary to prevent the depletion of the ionic liquid in the emitter chip with an array of deep-grooved emitters. Thus, we fabricated emitter chips with an array of deep-grooved emitters using an ionic liquid supply system, as described in Sections "Fabrication process of ionic liquid supply holes" and "Current measurements with an ionic liquid supply system", and measured the emission current.

Current–voltage characteristics with an ionic liquid supply system

Figure 14 shows the result of the ion emission experiment of the 81 deep-grooved emitter array with an ionic liquid supply system for different gap distances, where the hole aperture of the extractor electrode was $\varphi = 0.4$ mm for all cases. The horizontal axis is the voltage applied to the emitter chip, considering the voltage drop across the protective resistor (1 MΩ).

Figure 14a and b shows the current–voltage characteristics at a gap distance of $d = 0.4$ mm for the first and second voltage applications, respectively. As shown in Fig. 14b, on the positive side, the onset voltages of ion emission were 1540 V, and the maximum emitter current reached 717 μA at 2283 V. On the negative side, the onset voltages of ion emission were -1500 V and the minimum emitter current reached -716 μA at -2284 V. These values were almost the same as those at the first voltage application and stable current–voltage characteristics were observed for both voltage applications. Ionic-liquid depletion, as shown in Fig. 11c, was no longer observed when the ionic liquid was supplied from the back side of the emitter chip, and the slope of the current–voltage curves did not decrease, even when high voltages were applied. Compared with the results of the shallow-grooved emitters, the onset voltages of ion emission decreased on the positive side by approximately 320 V and increased on the negative side by approximately 360 V. The decrease was also partly attributed to the decrease in the distance between the extractor and emitter tip, as described in Section "Fabrication process of the emitters". Moreover, the absolute maximum emitter current of the deep-grooved emitters was more than three times that of the shallow-grooved emitters.

However, this result shows that deepening the grooves also increases the percentage of current interrupted by the extractor electrode about ten times. The percentage of current intercepted by the extractor electrode was 34% on the positive side at the voltage of the maximum emitter current, and 32% on the negative side at the voltage of the minimum emitter current. An ion beam spreading semi-angle θ can be estimated from the following equation:
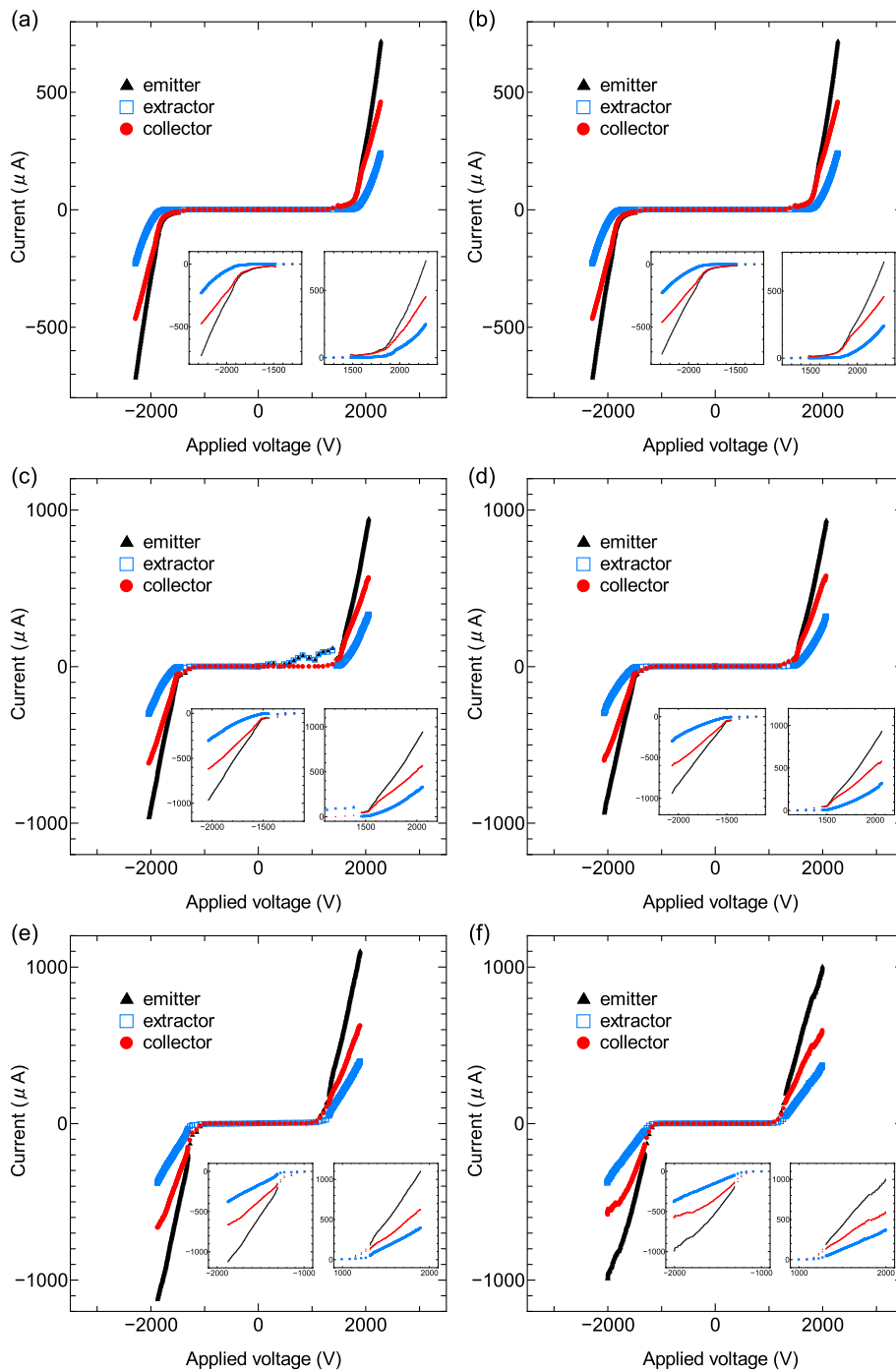
Fig. 14 Emitter, extractor, and collector currents of the 81 deep-grooved emitters with the ionic liquid supply system as functions of the applied voltage for different gap distances: **a**, **b** $d = 0.4$; **c**, **d** $d = 0.3$; and **e**, **f** $d = 0.2$ mm, where **a**, **c** and **e** are the results of the first measurement and **b**, **d** and **f** are those of the second measurement. The extractor electrode has an aperture of $\varphi = 0.4$ mm for all the cases. The bottom right insets of each figure represent zoomed views of the non-zero current section parts

$$\theta = \tan^{-1}\frac{9}{2}\left(\frac{I}{2\pi\varepsilon_0}\sqrt{\frac{m}{2q}}\phi_B^{-3/2}\right)^{1/2} \tag{1}$$

where I is the current, ε_0 is the permittivity of vacuum, m is the particle mass, q is the particle electric charge, and ϕ_B is the beam potential [51]. A limit angle not intercepted by the extractor electrode is 26.57° from the position relationship between the emitter tip and the extractor electrode, $d = 0.4$ mm and $\varphi = 0.4$ mm, assuming that all ions were emitted from the emitter tip. The maximum voltage, which did not exceed the limit angle, was 1822 V (the current was 67.7 μA) from the ion emission experiment with the deep-grooved emitter. Here, the angle θ was calculated to be 26.12° using Eq. (1). Therefore, no extractor currents were observed. However, the percentage of the current intercepted by the extractor electrode at 1822 V was 10%, as shown in Fig. 14b. This estimation suggests that the ions were also emitted from emission points other than the emitter tips. Thus, the results of an increase in the current intercepted by the extractor electrode with the deep-grooved emitters are probably due to the electric field concentrated on both emitter tips and protuberances on the emitter sides (i.e., ions could be emitted from these points).

We decreased the gap distance and performed current measurements to reduce the extractor current. Figure. 14c and d show the current–voltage characteristics at $d = 0.3$ mm for the first and second voltage applications, respectively. As shown in Fig. 14c, the current–voltage characteristics are slightly unstable, and an electrical short circuit appears only on the positive side before the onset voltage. The reason for this behavior remains unclear in this experiment, but a stable ion emission was obtained after the onset voltage. As shown in Fig. 14d, for $d = 0.3$ mm, the onset voltages of ion emission were 1280 V, and the maximum emitter currents reached 932 μA at 2068 V on the positive side, whereas the onset voltages of ion emission were -1290 V, and the minimum emitter currents reached -936 μA at -2065 V on the negative side. Although the maximum current for the second voltage application slightly decreased compared with the first, stable current–voltage characteristics were obtained over the entire voltage range, and ionic liquid depletion was not observed, as shown in Fig. 11c.

Figure 14e and f show the current–voltage characteristics at $d = 0.2$ mm for the first and second voltage applications, respectively, where stable current–voltage characteristics were obtained for both applications, although the emitter current for the second voltage application decreased at high voltages compared with the first voltage application. As shown in Fig. 14f, for $d = 0.2$ mm, the onset voltage of ion emission was 990 V, and the maximum emitter currents reached 1002 μA at 1996 V on the positive side, whereas the onset voltage of ion emission was -990 V, and the minimum emitter currents reached at -990 μA at -2007 V on the negative side. The maximum current per emitter exceeded 10 μA, and this very high current per emitter significantly consumed the ionic liquid in the tank, implying a slight depletion of the ionic liquid and a more sufficient supply system would be required.

The absolute onset voltage of ion emission decreases as the gap distance decreases and the maximum current increases because of the stronger electric field between the emitter and the extractor electrode. Compared with Fig. 11, more stable ion emission characteristics were obtained with the ionic liquid supply system for the externally wetted emitters. However, the percentage of current intercepted by the extractor electrode did not improve even when reducing the gap distances to $d = 0.2$ mm, indicating the need to optimize the deep-grooved emitter shape. The protuberances on the emitter sides

should be removed or placed close to the emitter bottom such that the electric field concentrates only on the emitter tips to prevent an increase in the percentage of current intercepted by the extractor electrode for deep-grooved emitters. The emitter should be fabricated in a conical shape [52, 53], which is left for future work.

Effects of hydraulic impedance

Electrospray phenomena are highly dependent on the hydraulic impedance [20, 21]. This study aims to increase the emission current by reducing the hydraulic impedance using a longitudinal groove on the emitter. It is challenging to precisely obtain the hydraulic impedance of externally wetted emitters because the impedance is significantly dependent on the wettability of the emitter surface and the film thickness of the ionic liquid. Mair [54] investigated the effects of hydraulic impedance on the current–voltage characteristics of externally wetted emitters for liquid metal ion sources, where the impedance was incorporated into the model for current–voltage curves based purely on space-charge considerations. The current–voltage model cannot be used for ionic liquid electrospray sources because the current is not controlled by the space charge [55]; thus, we only used the impedance depending on the structure to discuss the current–voltage characteristics for three emitters: non-grooved [36], shallow-grooved, and deep-grooved emitters.

When the length and radius of the needles are the same, the ratio of the hydraulic impedance of needles with smooth surfaces (non-grooved) to that of needles with grooved surfaces is obtained from the following equation (see Eqs. (8*d*) and (14*d*) of Ref. [54]):

$$\frac{3\pi}{64}\left(\frac{r}{\delta}\right)^3, \tag{2}$$

Where δ is the film thickness of the ionic liquid surrounding the needle and r is the radius of the longitudinal grooves, which are assumed to be semi-cylindrical in shape and separated by a distance of $2r$. The accurate film thickness δ could not be measured, but it should be less than 1 μm to have a stable ion emission based on the SEM and high-speed microscope images. The radii of the longitudinal shallow- and deep-grooves are estimated to be approximately 3 and 18 μm, respectively, based on the SEM images (Fig. 4). Even though δ is set to 1 μm, the ratio of the hydraulic of non-grooved emitters to that of shallow-grooved emitters is calculated to be approximately 4, and the ratio of the hydraulic of non-grooved emitters to that of deep-grooved emitters is approximately 860. These values significantly increase if the film thickness is less than 1 μm. Although these hydraulic impedances are rough estimates, the grooved structure decreased the hydraulic impedance, and the deep-grooved structure further decreased the impedance. The decrease in hydraulic impedance could explain the increase in current due to the grooving structure.

Discussion about electrochemical reactions

Electrochemical reactions caused by the extraction of a single polarity from ionic liquid electrospray thrusters are suppressed by periodically alternating the voltage polarity at a certain frequency, which can be estimated from the magnitude of the electrochemical

window of the ionic liquid [56]. In other words, the potential difference across the double layer formed between the emitter conductive material and the liquid must be maintained below the electrochemical window limit. Electrochemical reactions may damage emitters. Thus, it is crucial to consider the time, $t_W^{\pm}$, taken to lead the potential to the positive side or negative side of the electrochemical window limit, $V_W^{\pm}$, as given by the following equation [56]:

$$t_W^{\pm} = \varepsilon \varepsilon_0 \frac{V_W^{\pm}}{I} \frac{A}{\delta} \tag{3}$$

where ε is the dielectric constant of the ionic liquid, and A and δ are the effective area and thickness of the double-layer interface, respectively.

The time, $t_W^{\pm}$, can be roughly estimated from Eq. (3) using the obtained current–voltage characteristics, where for EMI-DCA, the electrochemical window has a value of $V_W^{-} \approx 1.2$ V [57], and the dielectric constant ε is 11.0 [58]. The thickness of the effective double layer is estimated as $\delta \approx 4.80 \times 10^{-10}$ m (approximate size of $[DCA]^{-}$) because the double layer is formed by $[DCA]^{-}$ anions placed very close to the conductor surface in the positive mode [59]. The effective double layer interface area for each emitter is estimated as $A \approx 3.9 \times 10^{-5}$ m^2 for the non-grooved emitter, $A \approx 4.1 \times 10^{-5}$ m^2 for the shallow-grooved emitter, and $A \approx 4.3 \times 10^{-5}$ m^2 for the deep-grooved emitter. The area is the sum of the approximate surface area of each emitter and the 6×6 mm^2 ionic liquid reservoir area where the ionic liquid was spread. By calculating the time, t_W^{-}, from these values using the current values at about 2200 V for each emitter, we get $t_W^{-} \approx 2.2$ s for the non-grooved emitter with $I = 4.31$ μA [36], $t_W^{-} \approx 0.31$ s for the shallow-grooved emitter with $I = 32.6$ μA (Fig. 11b) and $t_W^{-} \approx 0.018$ s for the deep-grooved emitter with $I = 570$ μA (Fig. 14b). These estimation results indicate that the voltage application at an alternation frequency of 1 Hz in our experiment with grooved emitters was not sufficient to suppress electrochemical reactions. Slight and distinctive brownish depositions were confirmed for the shallow- and deep-grooved emitter arrays, respectively, after the current measurements. In this study, ion-emission experiments with grooved emitters were conducted under the same conditions as those used in our previous study for comparison [36]. Experiments at higher alternation frequencies and the addition of an
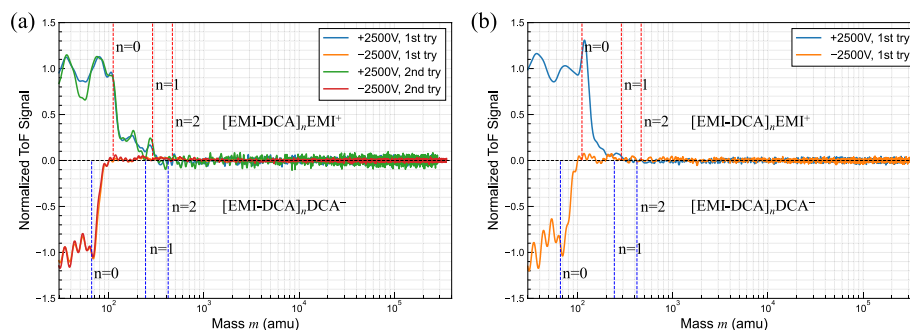

Fig. 15 Normalized ToF measurement results for **a** the shallow-grooved and **b** the deep-grooved emitter array

insulating layer to the Si emitters to suppress electrochemical reactions are left for future studies.

Time-of-flight measurements

ToF measurements were conducted for the emitter chips with 81 shallow-grooved emitters (Fig. 4b) and 81 deep-grooved emitters (Fig. 4c). The voltage applied to the emitter was different from that in the current–voltage measurements. The emitter voltage started at 1500 V and was increased by 10 V for 1 s to the measured voltage, which was fixed for a few 10 s at a constant polarity to obtain the averaged ToF signals. After the raw data were obtained, the data were filtered using a Butterworth filter [30]. Finally, the current is normalized to the average of the total current obtained before the gate voltage is applied.

Figure 15a shows the typical ToF spectra for the 81 shallow-grooved emitter chip at the source meter voltage of ± 2500 V for the first and second measurements. ToF signals are displayed as functions of the calculated species mass. Vertical dashed lines represent locations of monomer ($n=0$), dimer ($n=1$), and trimer ($n=2$) masses: [EMI-DCA]$_n$EMI$^+$ for cations and [EMI-DCA]$_n$DCA$^-$ for anions. In the figure, the difference between the first and second measurements is almost negligible. Although it was difficult to obtain the precise composition ratios for the ion beam because of the low signal-to-noise ratio, high ionic emissions were confirmed for both the first and second measurements. Currents of trimers, higher multimers, and droplets were not observed for cations, whereas those of dimers or higher multimers were not detected for anions. This tendency is probably due to the relatively high electrical conductivity and surface tension of EMI-DCA.

Figure 15b shows the typical ToF spectra for the 81 deep-grooved emitter chip at the source meter voltage of ± 2500 V for the first measurement. We could not obtain a good signal-to-noise ratio for the second and subsequent iterations. The current of the deep-grooved emitters without the ionic liquid supply system significantly decreased because of the ionic liquid depletion, as shown in Fig. 11d. In the ToF measurements, a longer voltage application was required to obtain a high signal-to-noise ratio. The emitter current was too low for the second ToF measurement. Similar to the ToF results of the shallow-grooved emitter, the currents of trimers, higher multimers, and droplets were not observed for cations, and those of dimers or higher multimers were not detected for anions.

Nonzero slopes between monomers and dimers appear in the cation results for both shallow- and deep-grooved emitters, implying fragmentation of dimers during the acceleration between the emitter and the extractor grid. However, it is difficult to obtain precise fragmentation ratios because of low signal-to-noise ratios. The ToF results indicated that the ion beams for both the shallow- and deep-grooved emitters were in the pure-ion regime, even for the first measurement, where we were unable to observe a difference between the first and second ion emission measurements (i.e., between the unstable and stable emission characteristics). The ToF results were obtained only at the centerline of the beams; thus, we investigated the difference in the ion beam emission between the first and second or subsequent times using a high-speed microscope.
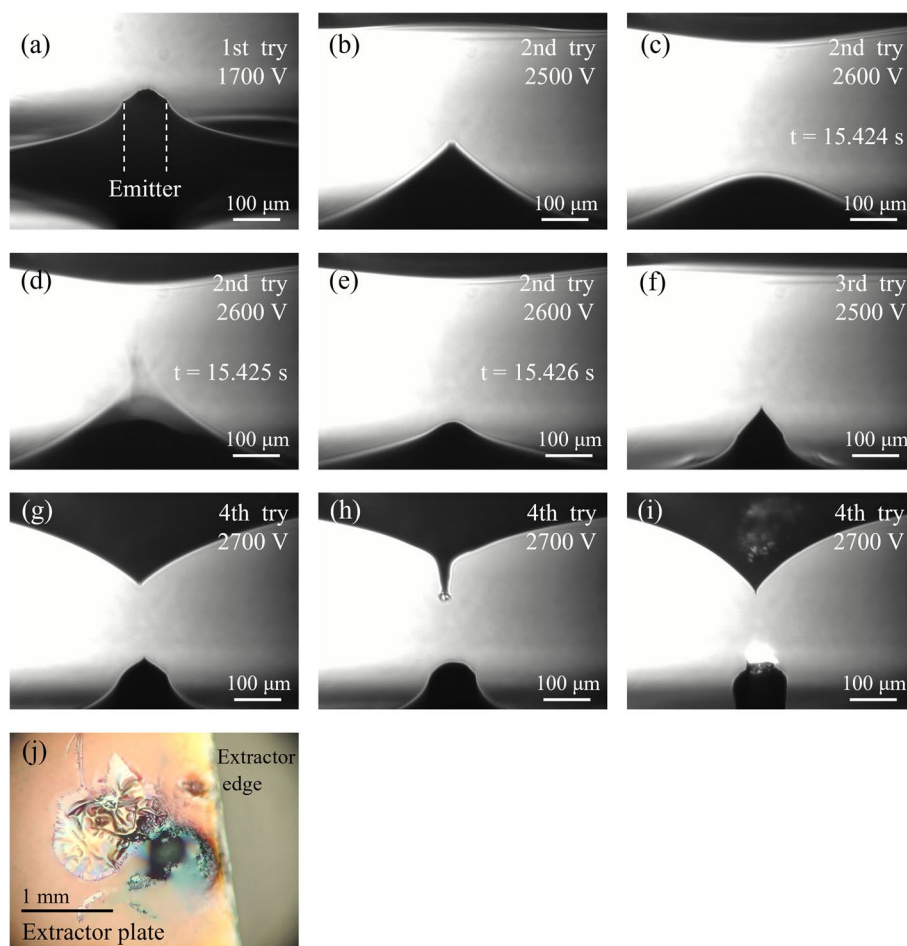
Fig. 16 Photograph images of high-speed microscope observation for a single emitter: **a** the first high-voltage application at 1700 V, **b** the second high-voltage application at 2500 V, and **c-e** 2600 V within 2 ms, **f** the third high-voltage application at 2500 V, and **g-i** the fourth high-voltage application at 2700 V. **i** The optical microscope photograph of the extractor plate after the extraction experiment

High-speed microscope observation

As a reference, a high-speed microscope was used to observe the extraction motion of the non-grooved single emitter. Figure 16 shows snapshots of the high-speed microscopic observations of the ionic liquid extracted from the emitter. In this case, the ionic liquid almost entirely covered the emitter electrode because the amount of ionic liquid was considerably large, as shown in Fig. 16a. The snapshots consist of four trial observations. As the voltage increased, the ionic liquid surrounding the emitter deformed into a Taylor cone shape in a steady state, as shown in Fig. 16b. The ionic liquid moved with the voltage alternation, and an unstable electrospray pulsation mode was occasionally observed, as illustrated in Fig. 16c-e. Pulsation occurred within 2 ms, which was also observed on a similar time scale in a capillary emitter [37]. Because all the emitted charged particles were collected at the extractor electrode without extraction holes, the ionic liquid was deposited on the extractor surface from the emitter surface. The ionic liquid on the emitter chip decreased after the second observation, as shown in Fig. 16f. The deposited ionic liquid on the extractor was also deformed into a Taylor cone shape
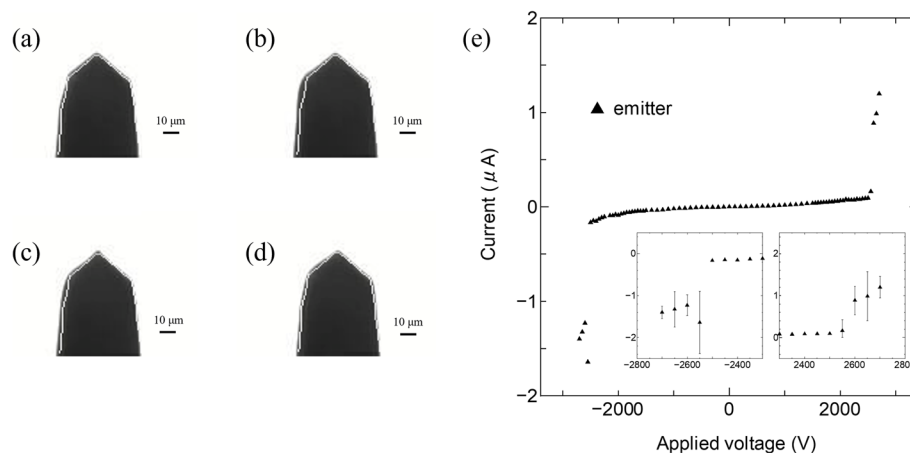
Fig. 17 Photograph images of high-speed microscope observation for the shallow-grooved 169-emitter array of the first high-voltage application at **a** − 2500, **b** 2550, **c** − 2550, and **d** 2600 V, where the outline of the emitter shape without ionic liquid is overlaid as a white line for each photograph. **e** The emitter current as a function of the applied voltage, together with insets representing zoomed views of the non-zero current section parts

owing to the electric field; thus, backspray phenomena were observed (Fig. 16g), which is considered one of the failure modes of the electrospray thruster [60]. A similar but much larger-scale dendritic growth of the ionic liquid was observed when the voltage was held at 2700 V for a while (several seconds), as shown in Fig. 16h [61]. Finally, a discharge occurred between the emitter and the deposited ionic liquid on the extractor, as shown in Fig. 16i. After the experiment, a solidified ionic liquid was observed on the extractor surface (Fig. 16j).

Following the trial observation of a single emitter, we observed the ion emissions of the shallow- and deep-grooved emitters. Figure 17 shows snapshots of the high-speed microscopy observations of one of the 169 shallow-grooved emitters at the first high-voltage application, together with current–voltage characteristics. The error bars represent the standard deviations of the measured current values. The larger error was attributed to ion emissions only from a single emitter out of the 169 emitters, not from all 81 emitters, as shown in Fig. 11, where ion emissions from many emitters decreased the deviation. The slight current slope at low voltages was due to the capacitive coupling induced by the voltage swing. We could not use the same cables as those used for the current measurements because of the limited space in the experimental setup. When the absolute voltage was 2500 V or less, ion emission was undetected, and the high-speed microscopy images showed no changes, as shown in Fig. 17a. When the voltage reached 2550 V, a slight increase in the volume of the ionic liquid was observed at the side edge of the emitter (Fig. 17b); however, ion emission was still undetectable. When the voltage was switched to − 2550 V, a tiny Taylor-cone shape was observed at the tip (Fig. 17c), and the abrupt negative ion emission was confirmed in Fig. 17e, where the absolute emission current reached the maximum. At an absolute voltage of 2600 V or higher, the high-speed microscope images did not change and were almost identical to those in Fig. 17d. The absolute current increased as the applied voltage increased.
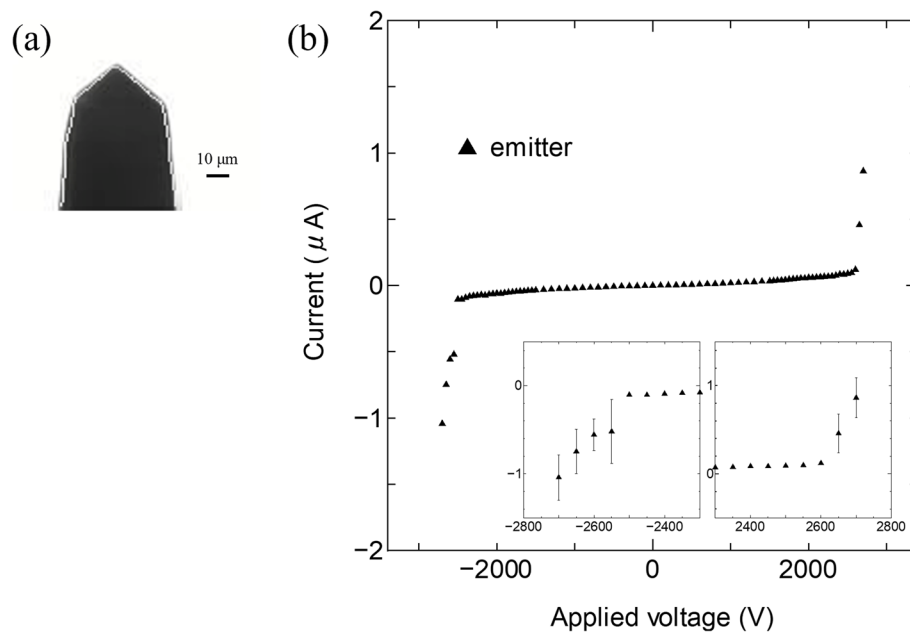
Fig. 18 a Photograph image of high-speed microscope observation for the shallow-grooved 169-emitter array of the fourth high-voltage application at 2600 V, where the outline of the emitter shape without ionic liquid is overlaid as a white line. **b** The emitter current as a function of the applied voltage, together with insets representing zoomed views of the non-zero current section parts

The current–voltage characteristics still exhibited an abrupt increase at the emission onset voltage for the second and third high-voltage applications. Because the ionic liquid was only extracted from the single emitter facing the extractor electrode, the ionic liquid deposited on the emitter array was probably pulled to that emitter, and a larger amount of ionic liquid was fed to it than in regular operation, as shown in Fig. 11b. Figure 18 shows a snapshot of the high-speed microscopic observation of one of the 169 shallow-grooved emitters at the fourth high-voltage application, together with the current–voltage characteristics. The images were displayed at a voltage of 2600 V. The high-speed microscope images showed no changes during the ion emission, and we had relatively stable current–voltage characteristics, where no abrupt increase in the emission current was observed. We did not observe a clear Taylor-cone shape during ion emission. The image in Fig. 18a is nearly identical to that in Fig. 17a. The emission site should be at the emitter tip; however, this is probably below the resolution of the present high-speed microscope.

Compared with the current–voltage characteristics shown in Fig. 11a and b, the absolute onset voltages were large by more than 600 V for the high-speed microscope observation setup. The emission current is also slightly lower than the current per emitter obtained in Fig. 11a and b. These discrepancies could be due to the difference in the alignment system, where one corner of the extractor could not be held, as shown in Fig. 10b, and the electrical contact with the extractor was attached to the farthest side from the observation point. The contact connection was probably too tight; thus, the gap distance between the extractor and emitter seemed larger than that used in Section "Current–voltage characteristics without an ionic liquid supply system".
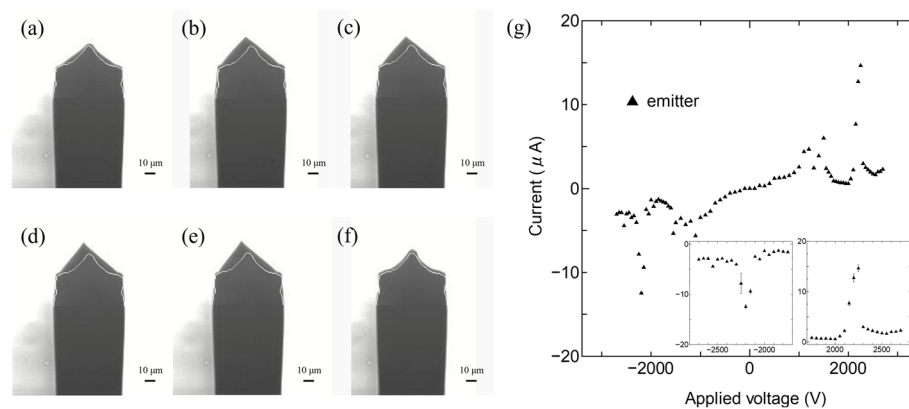
Fig. 19 Photograph images of high-speed microscope observation for the deep-grooved 169-emitter array of the first high-voltage application at **a** 2000, **b** 2100, **c** − 2100, **d** 2250, **e** − 2200, and **f** 2400 V, where the outline of the emitter shape without ionic liquid is overlaid as a white line for each photograph. **g** The emitter current as a function of the applied voltage, together with insets representing zoomed views of the non-zero current section parts

Figure 19 shows snapshots of the high-speed microscopic observations of one of the 169 deep-grooved emitters at the first high-voltage application, together with the current–voltage characteristics. Figure 19g illustrates the unstable current–voltage characteristics, in which some abrupt increases or decreases with large error bars in the emission currents were measured. Small currents were detected even at a few 100 V, which must be below the onset voltage for a gap distance of $d = 0.4$ mm. An electrical short-circuit may have occurred in these voltage ranges. Sudden increases in absolute currents were measured between ± 1000 and ± 1600 V. However, we could not observe high-speed microscope images in these voltage ranges, as mentioned in Section "Emission observation with a high-speed microscope". We cannot see what occurred without the images, but the surge current might have eliminated the pass of the electrical short circuit because we obtained almost zero currents between ± 1700 and ± 2000 V. In these voltage ranges, the high-speed microscopy images showed no changes (Fig. 19a), where the ionic liquid was fed to the slope of the emitter tip, but no Taylor-cone shapes were observed. When the voltage reached ± 2100 V, a Taylor-cone shape was observed at the emitter tip, but the direction was slightly tilted from the center line, as shown in Fig. 19b and c. When the voltage reached 2250 or − 2200 V, where the absolute current became the maximum for positive and negative sides, respectively, a clear Taylor-cone shape was observed at the tip, but the direction was still slightly tilted from the center line, as shown in Fig. 19d and e. This result can be attributed to the excess ionic liquid on the emitter for the first voltage application, as described in Section "Current measurements without an ionic liquid supply system". At an absolute voltage of 2300 V or above, the high-speed microscope images did not change and were almost identical to those shown in Fig. 19f (taken at 2400 V), where the emission current abruptly decreased, as shown in Fig. 11c, indicating the depletion of the ionic liquid. Although the current–voltage characteristics were unstable, as shown in Fig. 19g, no droplet extraction was observed.
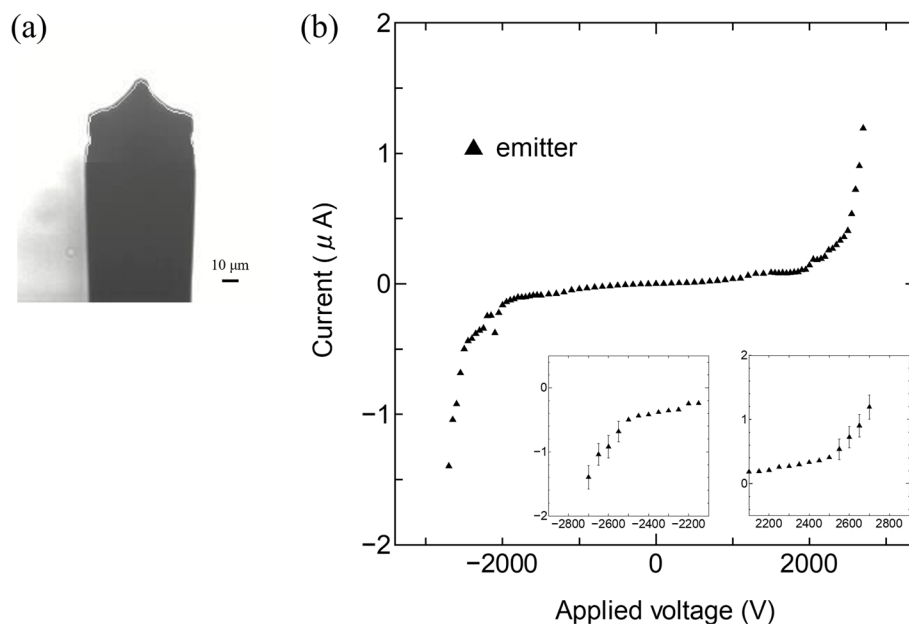
Fig. 20 a Photograph image of high-speed microscope observation for the deep-grooved 169-emitter array of the third high-voltage application at 2500 V, where the outline of the emitter shape without ionic liquid is overlaid as a white. **b** The emitter current as a function of the applied voltage, together with insets representing zoomed views of the non-zero current section parts

The second high-voltage application indicates unstable current–voltage characteristics for the same reason as described for shallow-grooved emitters. Figure 20 shows a snapshot of the high-speed microscopic observation of one of the 169 deep-grooved emitters at the third high-voltage application, together with the current–voltage characteristics. The images were displayed at a voltage of 2500 V. High-speed microscopic observations showed images almost identical to those in Fig. 20a during ion emission. Most of the extra ionic liquid should be extracted at this stage. We observed stable current–voltage characteristics, where no abrupt increase in emission currents was measured. However, we did not observe a clear Taylor-cone shape during ion emission. The emission site is probably below the resolution of the current high-speed microscope. Thus, we could not determine whether the emission sites also appeared at the protuberances on the emitter side.

Compared with the current–voltage characteristics shown in Fig. 11c and d, the absolute onset voltages were slightly large by approximately 200 V for the high-speed microscope observation setup. This discrepancy is also attributed to the same reason as that described for shallow-grooved emitters, but the contact connection was slightly loosened such that the gap distance was close to $d = 0.4$ mm. The emission current was slightly higher than the current per emitter, as shown in Fig. 11c and d, which can be attributed to the difference in the amount of ionic liquid per emitter. However, high-speed microscope observation also indicated that a larger amount of ionic liquid resulted in unstable current–voltage characteristics, whereas stable operation was realized with an appropriate supply of ionic liquid.

Notably, we observed only one side of the emitter due to the limitations of the present observation setup. The Taylor cone at the side edge may have been observed at the front

or back of the emitter, which the microscope could not observe. Although such emission sites might have resulted in a large extractor current for the deep-grooved emitters, high-speed microscope observations indicated that no large droplets (> a few micrometers in diameter) were emitted for either grooved emitter structure, at least in the beam center line, which is consistent with the ToF results. The angle dependence of the ToF measurement will be investigated in future studies.

Conclusions

In this study, we fabricated externally wetted needle-shaped emitters with a longitudinally grooved structures for use in ionic liquid electrospray thrusters to improve the transport of ionic liquids to emitter tips. Two types of grooved shapes with different groove depths (i.e., shallow- and deep-grooved emitters) were successfully fabricated using a star-shaped etching mask and by changing the mask diameter and etching time. Additionally, through-holes were fabricated at the base of the deep-grooved emitters to supply the ionic liquid from the back side of the emitter chips.

The first current–voltage measurement without an ionic liquid supply system showed unstable characteristics because of oversupply of the ionic liquid. This instability was reduced in the second and subsequent trials using the ionic liquid supply system with through-holes. Ion emission experiments showed that the absolute emission current increased with grooved needle emitters compared with non-grooved needle emitters in our previous study. This tendency became stronger with deeper grooves, which is attributed to the low hydraulic impedance of the emitter structure. Moreover, the slope of current–voltage curve did not change even at high voltages with grooved emitters. These results indicate that grooving improves ionic liquid transport to emitter tips. However, deeper grooving also increased the percentage of current intercepted by the extractor electrode, probably because the electric field was concentrated on both the emitter tips and the protuberances on the emitter sides. Electrochemical reactions were not avoided at an alternation frequency of 1 Hz due to high emission currents, implying the need for higher-frequency operation and the addition of an insulating layer to the Si emitters. The ToF spectrometry was also conducted, and the results indicated that the emission at the centerline was in the pure-ion regime, including mostly monomer and dimer ions, under all measured conditions. High-speed microscopy observations showed that too much ionic liquid deposited on the extractor caused backspray and implied no large droplet emission in the centerline of the beams for both grooved emitters, which is consistent with the ToF results.

In future work, we plan to fabricate deep-grooved emitters that are closer to a conical shape by moving the protuberances on the emitter sides to the bottom of the emitter using grayscale lithography. Additionally, future work will include voltage applications with higher alternation frequencies and the investigation of angle dependencies in ToF measurements. A ToF system using a longer flight length and an electron multiplier instead of a high-speed current amplifier will also be developed to investigate ion beam compositions and fragmentation.

Matsukawa *et al. Journal of Electric Propulsion*   (2023) 2:23

Page 26 of 28

Availability of data and materials

The datasets generated and analyzed in the current study are available from the corresponding author upon reasonable request.

Declarations

Competing interests

The authors declare that they have no competing interests.

References

1. Amaro Seoane P, Arca Sedda M, Babak S, Berry CPL, Berti E, Bertone G, Blas D, Bogdanović T, Bonetti M, Breivik K, Brito R, Caldwell R, Capelo PR, Caprini C, Cardoso V, Carson Z, Chen H-Y, Chua AJK, Dvorkin I, Haiman Z, Heisenberg L, Isi M, Karnesis N, Kavanagh BJ, Littenberg TB, Mangiagli A, Marcoccia P, Maselli A, Nardini G, Pani P, Peloso M, Pieroni M, Ricciardone A, Sesana A, Tamanini N, Toubiana A, Valiante R, Vretinaris S, Weir DJ, Yagi K, Zimmerman A (2022) The effect of mission duration on LISA science objectives. Gen Relativ Gravit 54(1):3. https://doi.org/10.1007/s10714-021-02889-x
2. Kawamura S, Ando M, Seto N, Sato S, Musha M, Kawano I, Yokoyama Ji, Tanaka T, Ioka K, Akutsu T, Takashima T, Agatsuma K, Araya A, Aritomi N, Asada H, Chiba T, Eguchi S, Enoki M, Fujimoto M-K, Fujita R, Futamase T, Harada T, Hayama K, Himemoto Y, Hiramatsu T, Hong F-L, Hosokawa M, Ichiki K, Ikari S, Ishihara H, Ishikawa T, Itoh Y, Ito T, Iwaguchi S, Izumi K, Kanda N, Kanemura S, Kawazoe F, Kobayashi S, Kohri K, Kojima Y, Kokeyama K, Kotake K, Kuroyanagi S, Maeda K-i, Matsushita S, Michimura Y, Morimoto T, Mukohyama S, Nagano K, Nagano S, Naito T, Nakamura K, Nakamura T, Nakano H, Nakao K, Nakasuka S, Nakayama Y, Nakazawa K, Nishizawa A, Ohkawa M, Oohara K, Sago N, Saijo M, Sakagami M, Sakai S-i, Sato T, Shibata M, Shinkai H, Shoda A, Somiya K, Sotani H, Takahashi R, Takahashi H, Akiteru T, Taniguchi K, Taruya A, Tsubono K, Tsujikawa S, Ueda A, Ueda K-i, Watanabe I, Yagi K, Yamada R, Yokoyama S, Yoo C-M, Zhu Z-H (2021) Current status of space gravitational wave antenna DECIGO and B-DECIGO. Progress of Theoretical and Experimental Physics 2021(5):05A105. https://doi.org/10.1093/ptep/ptab019
3. Simone D'Amico AK (2019) Bruce Macintosh System Design of the Miniaturized Distributed Occulter/Telescope (mDOT) Science Mission In: 33rd Annual Small Satellite Conference, Logan, Utah, SSC19-IV-08
4. Thibault LBF, Daniel PS, Carl RS, Michael B, Stefan RM (2020) Starshade formation flying II: formation control. Journal of Astronomical Telescopes, Instruments, and Systems 6(2):029001. https://doi.org/10.1117/1.JATIS.6.2.029001
5. Ziemer JK, Marrese-Reading C, Arestie S, Demmons NR, Wirz RE, Collins A, Gamero M (2020) Progress on Developing LISA Microthruster Technology In: AIAA Propulsion and Energy 2020 Forum, Online, AIAA 2020–3609. https://doi.org/10.2514/6.2020-3609
6. Scharlemann C, Buldrini N, Killinger R, Jentsch M, Polli A, Ceruti L, Serafini L, DiCara D, Nicolini D (2011) Qualifciation test series of the indium needle FEEP micro-propulsion system for LISA Pathfinder. Acta Astronaut 69(9):822–832. https://doi.org/10.1016/j.actaastro.2011.05.037
7. Bandyopadhyay S, Foust R, Subramanian GP, Chung S-J, Hadaegh FY (2016) Review of Formation Flying and Constellation Missions Using Nanosatellites. J Spacecr Rockets 53(3):567–578. https://doi.org/10.2514/1.A33291
8. Klesh AT, Baker J, Krajewski J (2019) MarCO: Flight Review and Lessons Learned In: 33rd Annual AIAA/USU Conference on Small Satellites, Logan, Utah, SSC19-III-04
9. Funase R, Ikari S, Miyoshi K, Kawabata Y, Nakajima S, Nomura S, Funabiki N, Ishikawa A, Kakihara K, Matsushita S, Takahashi R, Yanagida K, Mori D, Murata Y, Shibukawa T, Suzumoto R, Fujiwara M, Tomita K, Aohama H, Iiyama K, Ishiwata S, Kondo H, Mikuriya W, Seki H, Koizumi H, Asakawa J, Nishii K, Hattori A, Saito Y, Kikuchi K, Kobayashi Y, Tomiki A, Torii W, Ito T, Campagnola S, Ozaki N, Baresi N, Yoshikawa I, Yoshioka K, Kuwabara M, Hikida R, Arao S, Abe S, Yanagisawa M, Fuse R, Masuda Y, Yano H, Hirai T, Arai K, Jitsukawa S, Ishioka E, Nakano H, Ikenaga T, Hashimoto T (2020) Mission to Earth-Moon Lagrange Point by a 6U CubeSat: EQUULEUS. IEEE Aerosp Electron Syst Mag 35(3):30–44. https://doi.org/10.1109/MAES.2019.2955577
10. Romero-Sanz I, Bocanegra R, Fernandez de la Mora J, Gamero-Castaño M (2003) Source of heavy molecular ions based on Taylor cones of ionic liquids operating in the pure ion evaporation regime. J Appl Phys 94(5):3599–3605. https://doi.org/10.1063/1.1598281

Matsukawa *et al. Journal of Electric Propulsion*   (2023) 2:23

Page 27 of 28

11.   Lozano P, Martínez-Sánchez M (2005) Ionic liquid ion sources: characterization of externally wetted emitters. J Colloid Interface Sci 282(2):415–421. https://doi.org/10.1016/j.jcis.2004.08.132

12.   Krpoun R, Smith KL, Stark JPW, Shea HR (2009) Tailoring the hydraulic impedance of out-of-plane micromachined electrospray sources with integrated electrodes. Appl Phys Lett 94(16):163502–1–3. https://doi.org/10.1063/1.3117191

13.   Legge RS, Lozano PC (2011) Electrospray Propulsion Based on Emitters Microfabricated in Porous Metals. J Propul Power 27(2):485–495. https://doi.org/10.2514/1.50037

14.   Hill FA, Heubel EV, Leon PPd, Velasquez-Garcia LF (2014) High-Throughput Ionic Liquid Ion Sources Using Arrays of Microfabricated Electrospray Emitters With Integrated Extractor Grid and Carbon Nanotube Flow Control Structures. J Microelectromech S 23(5):1237–1248. https://doi.org/10.1109/JMEMS.2014.2320509

15.   Dandavino S, Ataman C, Ryan CN, Chakraborty S, Courtney D, Stark JPW, Shea H (2014) Microfabricated electrospray emitter arrays with integrated extractor and accelerator electrodes for the propulsion of small spacecraft. J Micromech Microeng 24(7):075011–1–13. https://doi.org/10.1088/0960-1317/24/7/075011

16.   Courtney DG, Dandavino S, Shea H (2016) Comparing Direct and Indirect Thrust Measurements from Passively Fed Ionic Electrospray Thrusters. J Propul Power 32(2):392–407. https://doi.org/10.2514/1.B35836

17.   Krejci D, Mier-Hicks F, Thomas R, Haag T, Lozano P (2017) Emission Characteristics of Passively Fed Electrospray Microthrusters with Propellant Reservoirs. J Spacecr Rockets 54(2):447–458. https://doi.org/10.2514/1.A33531

18.   Taylor G (1964) Disintegration of Water Drops in an Electric Field. Proc R Soc London A 280(1382):383–397. https://doi.org/10.1098/rspa.1964.0151

19.   Wilm MS, Mann M (1994) Electrospray and Taylor-Cone theory, Dole's beam of macromolecules at last? Int J Mass Spectrom Ion Process 136(2):167–180. https://doi.org/10.1016/0168-1176(94)04024-9

20.   Coffman CS, Martínez-Sánchez M, Lozano PC (2019) Electrohydrodynamics of an ionic liquid meniscus during evaporation of ions in a regime of high electric field. Phys Rev E 99(6):063108. https://doi.org/10.1103/PhysRevE.99.063108

21.   Gallud X, Lozano PC (2022) The emission properties, structure and stability of ionic liquid menisci undergoing electrically assisted ion evaporation. J Fluid Mech 933:A43. https://doi.org/10.1017/jfm.2021.988

22.   Gamero-Castaño M, Magnani M (2019) Numerical simulation of electrospraying in the cone-jet mode. J Fluid Mech 859:247–267. https://doi.org/10.1017/jfm.2018.832

23.   Kitazawa Y, Ueno K, Watanabe M (2018) Advanced Materials Based on Polymers and Ionic Liquids. Chem Record 18(4):391–409. https://doi.org/10.1002/tcr.201700041

24.   Natisin MR, Zamora HL, Holley ZA, Ivan Arnold N, McGehee WA, Holmes MR, Eckhardt D (2021) Efficiency Mechanisms in Porous-Media Electrospray Thrusters. J Propul Power 37(5):650–659. https://doi.org/10.2514/1.B38160

25.   Petro E, Bruno A, Lozano P, Perna LE, Freeman D (2020) Characterization of the TILE Electrospray Emitters In: AIAA Propulsion and Energy 2020 Forum, AIAA-2020–3612. https://doi.org/10.2514/6.2020-3612

26.   Hruby V, Demmons N, Courtney D, Ziemer J, Dunn C, Marrese-Reading C (2018) Colloid Micronewton Thrusters (CMNTs) – Comparison Between LISA Pathfinder In-Flight and Ground Measurements In: Space Propulsion 2018. SP2018_00567. https://www.3af-spacepropulsion.com/previous-editions

27.   Cisquella-Serra A, Galobardes-Esteban M, Gamero-Castaño M (2022) Scalable Microfabrication of Multi-Emitter Arrays in Silicon for a Compact Microfluidic Electrospray Propulsion System. ACS Appl Mater Interfaces 14(38):43527–43537. https://doi.org/10.1021/acsami.2c12716

28.   Liu X, He W, Kang X, Xu M (2019) Fabrication of porous emitters for ionic liquid ion source by wire electrical discharge machining combined with electrochemical etching. Rev Sci Instrum 90(12):123304. https://doi.org/10.1063/1.5099512

29.   Natisin MR, Zamora HL, McGehee WA, Arnold NI, Holley ZA, Holmes MR, Eckhardt D (2020) Fabrication and characterization of a fully conventionally machined, high-performance porous-media electrospray thruster. J Micromech Microeng 30(11):115021. https://doi.org/10.1088/1361-6439/abb8c3

30.   Ma C, Bull T, Ryan CN (2021) Plume Composition Measurements of a High-Emission-Density Electrospray Thruster. J Propul Power 37(6):816–831. https://doi.org/10.2514/1.B37996

31.   Dressler RA, St. Peter B, Chiu Y-H, Fedkiw T (2022) Multiple Emission Sites on Porous Glass Electrospray Propulsion Emitters Using Dielectric Propellants. J Propul Power 38(5):809–821. https://doi.org/10.2514/1.B38453

32.   Castro S, Fernández de la Mora J (2009) Effect of tip curvature on ionic emissions from Taylor cones of ionic liquids from externally wetted tungsten tips. J Appl Phys 105(3):034903. https://doi.org/10.1063/1.3073873

33.   Shingu T, Nagao M, Murakami K, Murata H, Khumpuang S, Hara S, Takao Y (2023) Fabrication and Demonstration of SU-8 Based Emitter Arrays for Ionic Liquid Electrospray Thrusters. Journal of Evolving Space Activities 1:30. https://doi.org/10.57350/jesa.30

34.   Suzuki K, Nagao M, Liu Y, Murakami K, Khumpuang S, Hara S, Takao Y (2021) Fabrication of nano-capillary emitter arrays for ionic liquid electrospray thrusters. Jpn J Appl Phys 60(SC):SCCF07–1–6. https://doi.org/10.35848/1347-4065/abf2d5

35.   Inoue N, Nagao M, Murakami K, Khumpuang S, Hara S, Takao Y (2019) Fabrication of a high-density emitter array for electrospray thrusters using field emitter array process. Jpn J Appl Phys 58(SE):SEEG04–1–7. https://doi.org/10.7567/1347-4065/ab0fee

36.   Tachibana F, Tsuchiya T, Takao Y (2021) Uniform needle-emitter arrays for ionic liquid electrospray thrusters with precise thrust control. Jpn J Appl Phys 60(SC):SCCL06–1–9. https://doi.org/10.35848/1347-4065/abe997

37.   Uchizono NM, Collins AL, Thuppul A, Wright PL, Eckhardt DQ, Ziemer J, Wirz RE (2020) Emission Modes in Electrospray Thrusters Operating with High Conductivity Ionic Liquids. Aerospace 7(10):141. https://doi.org/10.3390/aerospace7100141

38.   Thuppul A, Collins AL, Wright PL, Uchizono NM, Wirz RE (2021) Mass flux and current density distributions of electrospray plumes. J Appl Phys 130(10):103301. https://doi.org/10.1063/5.0056761

39.   Zhang K, Kuang S, Suo X, Huang X, Li Z, Wang D, Jia H, Tu L, Song P (2022) Analysis of beam currents under an oscillating cone-jet mode for developing high-precision electrospray thrusters. J Appl Phys 131(9):094501. https://doi.org/10.1063/5.0083210

40. Huang C, Li J, Li M, Si T, Xiong C, Fan W (2021) Experimental investigation on current modes of ionic liquid electrospray from a coned porous emitter. Acta Astronaut 183:286–299. https://doi.org/10.1016/j.actaastro.2021.03.014

41. Schroeder MR, Lozano PC (2022) Investigating Prompt Ionic Liquid Cluster Fragmentation from Electrospray Total Mass Flow Measurements In: the 37th International Electric Propulsion Conference, Massachusetts Institute of Technology, Cambridge, MA, USA, IEPC-2022–210

42. Roozeboom F, van den Bruele F, Creyghton Y, Poodt P, Kessels WMM (2015) Cyclic Etch/Passivation-Deposition as an All-Spatial Concept toward High-Rate Room Temperature Atomic Layer Etching. ECS J Solid State Sci Technol 4(6):N5067. https://doi.org/10.1149/2.0111506jss

43. Wu B, Kumar A, Pamarthy S (2010) High aspect ratio silicon etch: A review. J Appl Phys 108(5):051101. https://doi.org/10.1063/1.3474652

44. Nakagawa K, Tsuchiya T, Takao Y (2017) Microfabricated emitter array for an ionic liquid electrospray thruster. Jpn J Appl Phys 56(6S1):06GN18–1–8. https://doi.org/10.7567/JJAP.56.06GN18

45. Su L, Zhuo J, Liu H, Yao Z, Xu X, Li S (2023) Fragmentation modeling of gas-phase ionic liquid clusters in high-voltage electric field. Fuel 335:126919. https://doi.org/10.1016/j.fuel.2022.126919

46. Cook R, Nabity JA, Daily JW (2017) Characterizing Propellants for Variable-Thrust/Specific Impulse Colloid Thrusters. J Propul Power 33(6):1325–1331. https://doi.org/10.2514/1.B36495

47. Uchizono NM, Collins AL, Marrese-Reading C, Arestie SM, Ziemer JK, Wirz RE (2021) The role of secondary species emission in vacuum facility effects for electrospray thrusters. J Appl Phys 130(14):143301–1–21. https://doi.org/10.1063/5.0063476

48. Lyne CT, Liu MF, Rovey JL (2023) A simple retarding-potential time-of-flight mass spectrometer for electrospray propulsion diagnostics. J Electr Propuls 2(1):13. https://doi.org/10.1007/s44205-023-00045-y

49. Fujiwara Y (2023) Effects of the temperature of a protic ionic liquid on ion beam production by vacuum electrospray. J Vac Sci Technol B 41(2):024202. https://doi.org/10.1116/6.0002403

50. Lozano P, Martínez-Sánchez M (2005) On the dynamic response of externally wetted ionic liquid ion sources. J Phys D 38(14):2371. https://doi.org/10.1088/0022-3727/38/14/011

51. Lozano P, "Studies on the Ion-Droplet Mixed Regime in Colloid Thrusters," Ph. D. Thesis, Dept of Aeronautics and Astronautics, Massachusetts Institute of Technology, 2003

52. Corrado MN, Lozano PC, Parameswaran L, Cook M, Holihan EC, Mathews R, Racz LM, Smith MA (2022) Densification of Ionic Liquid Electrospray Thrusters using Silicon-Based MEMS Fabrication In: the 37th International Electric Propulsion Conference, Massachusetts Institute of Technology, Cambridge, MA, USA, IEPC-2022–177

53. Melissa AS, Shaun B, Lalitha P, Christopher H, Noah S, Ronald L, Michael PC, Daniel F, Mordechai R (2019) Design, simulation, and fabrication of three-dimensional microsystem components using grayscale photolithography. Journal of Micro/Nanolithography, MEMS, and MOEMS 18(4):043507. https://doi.org/10.1117/1.JMM.18.4.043507

54. Mair GLR (1997) The effects of flow impedance on the current - voltage characteristics of liquid-metal ion sources. J Phys D 30(13):1945. https://doi.org/10.1088/0022-3727/30/13/017

55. Higuera FJ (2008) Model of the meniscus of an ionic-liquid ion source. Phys Rev E 77(2):026308. https://doi.org/10.1103/PhysRevE.77.026308

56. Lozano P, Martínez-Sánchez M (2004) Ionic liquid ion sources: suppression of electrochemical reactions using voltage alternation. J Colloid Interface Sci 280(1):149–154. https://doi.org/10.1016/j.jcis.2004.07.037

57. Deng M-J, Chen P-Y, Leong T-I, Sun IW, Chang J-K, Tsai W-T (2008) Dicyanamide anion based ionic liquids for electrodeposition of metals. Electrochem Commun 10(2):213–216. https://doi.org/10.1016/j.elecom.2007.11.026

58. Hunger J, Stoppa A, Schrödle S, Hefter G, Buchner R (2009) Temperature Dependence of the Dielectric Properties and Dynamics of Ionic Liquids. ChemPhysChem 10(4):723–733. https://doi.org/10.1002/cphc.200800483

59. Luo J, Hong M, Weng J, Zhao Y, Cao R (2002) The complexes with end-to-end dicyanamide bridges: syntheses, characterization and crystal structures of [Cu(µ1,5-dca)2(phen)]n and [Cd(µ1,5-dca)2(py)2]n (phen=phenanthroline; py=pyridine; dca=dicyanamide, N(CN)2−). Inorg Chim Acta 329(1):59–65. https://doi.org/10.1016/S0020-1693(01)00794-0

60. Thuppul A, Wright PL, Collins AL, Ziemer JK, Wirz RE (2020) Lifetime Considerations for Electrospray Thrusters. Aerospace 7(8):108. https://doi.org/10.3390/aerospace7080108

61. Terhune KJ, King LB, He K, Cumings J Radiation-induced solidification of ionic liquid under extreme electric field. Nanotechnology 2016;27(37):375701. https://doi.org/10.1088/0957-4484/27/37/375701

Publisher's Note